Supplementary Information

Hierarchical Polar–Nonpolar Phase Architecture Enabling Excellent Lead-free Capacitive Energy Storage

Qingqing Wu[a], Huajie Luo[b]*, Yuhang Hu[a], Yuhui Huang[c], Xiangwei Guo[c]*, Hubo Zhu[a], Haishan Xu[a], Shenglin Jiang[d], Tianyu Li[e]*, Bing Xie[a]*

[a]School of Power and Energy, Jiangxi Key Laboratory of Green General Aviation Power, Nanchang Hangkong University, Nanchang 330063, China

[b]School of Materials Science and Engineering, University of Science and Technology Beijing, Beijing 100083, China

[c]State Key Laboratory of Silicon and Advanced Semiconductor Materials, School of Materials Science and Engineering, Zhejiang University, Hangzhou, Zhejiang 310058, China.

[d]School of Integrated Circuits, Huazhong University of Science and Technology, Wuhan 430074, China

[e]Department of Physics, City University of Hong Kong, Hong Kong SAR, China

Corresponding authors: xieb@nchu.edu.cn (Bing Xie); hjluo@ustb.edu.cn (Huajie Luo); l240441@zju.edu.cn (Xiangwei Guo) and tianyuli@ustb.edu.cn (Tianyu Li)

Materials and Methods

Sample preparation

$0.5BaTiO_3$–$(0.5–x)Bi(Mg_{0.5}Ti_{0.5})O_3$–$xCdZrO_3$ [0.5BT−(0.5−*x*)BMT−*x*CZ] ceramics, with $x = 0$, 0.1, 0.15, 0.2, and 0.25, were synthesized using the conventional solid-state reaction method. The starting materials included Bi_2O_3 (99.9%), TiO_2 (98%), CdO (99.9%), ZrO_2 (99.99%), MgO (99.8%), and $BaCO_3$ (99%) powders. The dried powders were weighed according to the stoichiometric ratios and ball-milled in anhydrous ethanol for 10 hours. The resulting mixture was dried and calcined in air at 780 °C for 2 hours. Subsequently, the calcined powder was mixed with polyvinyl alcohol (PVA) binder, thoroughly ground, and then pressed into pellets 10 mm in diameter and 1 mm thick. To minimize elemental volatilization during sintering, the pellets were covered with powder and sintered at 1050–1150 °C for 2 hours. To identify the optimal sintering temperature, we performed sintering experiments on the selected compositions at various temperatures. The corresponding microstructure and elemental analyses are presented in Figures S12 and S13. Within the temperature range of 1000–1100 °C, samples sintered at 1025 °C and 1050 °C exhibit uniform contrast and well-defined phase separation, whereas the sample sintered at 1000 °C shows inferior ceramic quality. Samples sintered between 1075 °C and 1100 °C display rough surfaces and noticeable precipitates, indicating that excessively high sintering temperatures adversely affect the grain-level microstructure. Meanwhile, grain size increases gradually with sintering temperature; however, no significant differences are observed between 1025 °C and 1050 °C. Energy-dispersive X-ray spectroscopy (EDS) analysis confirms that the phase separation pattern remains consistent across all temperatures, suggesting that the two-phase structure is governed by the reaction process rather than the sintering conditions. Considering grain size, sintering quality, and elemental distribution, the temperature range of 1025–1050 °C provides the optimal microstructural characteristics, with the best overall performance at 1050 °C. Therefore, 1050 °C was selected as the optimal sintering temperature for these ceramics. The relative densities of the ceramics, measured by the Archimedes method, exceeded 95% in all cases.

Characterization

The phase structure was characterized by X-ray diffraction (XRD) using a D8ADVANCE-A25 diffractometer (Bruker, Germany). Microstructure and elemental distribution analyses were conducted with a field-emission scanning electron microscope (FE-SEM; Zeiss Gemini SEM 300, Germany) equipped with energy-dispersive X-ray spectroscopy (EDS; Oxford Instruments X-MaxN SN 78861). Prior to SEM observation, all samples were polished and thermally etched at 1050–1150 °C for 0.5 hours. Selected area electron diffraction (SAED) patterns and high-resolution transmission electron microscopy (HRTEM) images were obtained using an aberration-corrected scanning transmission electron microscope (STEM; FEI Titan Cubed Themis G2 300, Thermo Fisher Scientific, USA) operating at 300 kV. Atomic-scale high-angle annular dark-field (HAADF) STEM images were acquired with a probe- and image-aberration-corrected microscope operated at 200 kV. All STEM images were Fourier-filtered using a lattice mask to reduce noise. The precise positions of the A- and B-site atomic columns were determined by fitting two-dimensional Gaussian functions, and the angles and magnitudes of polar displacements were calculated using a MATLAB script.

Polarization-electric field (*P–E*) loops under varying electric fields, frequencies, temperatures, and cycle numbers were measured using a ferroelectric test system (FETS-2000, Wuhan Yanhe Technology Co., Ltd., China). Breakdown strength was evaluated with a dielectric breakdown test system at a ramp rate of 500 V/s (PolyK Technologies, USA). Dielectric properties, including dielectric constant and loss, were characterized as functions of temperature (21–500 °C) and frequency (1 kHz–1 MHz) using the FETS-2000 system. Charge–discharge measurements were conducted on a charge–discharge test system (CCDM-1000, Wuhan Yanhe Technology Co., Ltd., China). Alternating current (AC) impedance spectroscopy was performed with an electrochemical workstation (CHI700e, CH Instruments, USA) over the temperature range of 410–570 °C. Ultraviolet–visible (UV-Vis) absorption spectra were recorded using a UV-Vis spectrometer (UV-9000, METASH, China) over the wavelength range of 200–800 nm, with BaSO4 employed as the reference material.

Phase-field simulations

Phase-field simulations were carried out to investigate the polarization evolution in 0.5BT−(0.5−x)BMT−xCZ bulk ceramic. The spontaneous polarization P_i (i = 1-3) are taken as the order parameters, whose temporal evolution is described by the time-dependent Ginzburg-Landau equation:

$$\frac{\partial P_i}{\partial t} = -L\frac{\delta F}{\delta \boldsymbol{P}} \tag{1}$$

Here, t represents the evolution time, and L is the kinetic coefficient associated with domain-wall mobility. The total free energy F of the bulk ceramic is expressed as the volume integral of several energy contributions, including bulk, gradient, elastic, and electrostatic terms[1]:

$$F = \int (f_{bulk}(P_i) + f_{grad}(P_{i,j}) + f_{elas}(P_i, \varepsilon_{ij}) + f_{elec}(P_i, E_i))\, dV \tag{2}$$

The bulk energy density is expressed as:

$$f_{bulk} = \alpha_{ij}P_iP_j + \alpha_{ijkl}P_iP_jP_kP_l + \alpha_{ijklmn}P_iP_jP_kP_lP_mP_n + \alpha_{ijklmnop}P_iP_jP_kP_lP_mP_nP_oP_p \tag{3}$$

where α_{ij}, α_{ijkl}, α_{ijklmn}, and $\alpha_{ijklmnop}$ denote the Landau coefficients. These coefficients are determined by linearly interpolating the corresponding parameters of constituent compounds BTO, BMT, and CZ.[2, 3] To incorporate concentration inhomogeneities, local fluctuations of the disordered concentration with magnitude of 0.3 are introduced.

The gradient energy density is given by:

$$f_{\text{grad}} = \frac{1}{2} g_{ijkl} P_{i,j} P_{k,l} \tag{4}$$

where g_{ijkl} denotes the gradient energy coefficient.

The elastic energy density is written as:

$$f_{\text{elas}} = \frac{1}{2} c_{ijkl}\left(\varepsilon_{ij} - \varepsilon_{ij}^0\right)\left(\varepsilon_{kl} - \varepsilon_{kl}^0\right) \tag{5}$$

where c_{ijkl} is the elastic stiffness tensor, ε_{ij} is the total strain. The eigenstrain ε_{ij}^0 is related to ferroelectric polarization P_i through $\varepsilon_{ij}^0 = Q_{ijkl}P_kP_l$, where Q_{ijkl} is the electrostrictive coefficient.

The electrostatic energy density is described as:

$$f_{\text{elec}}=-\frac{1}{2}\kappa_0\kappa_b E_i E_j - E_i P_i \quad (6)$$

where κ_0 is the permittivity of vacuum, κ_b is background relative dielectric constant, and E_i is the total electric field. The polarization−electric field (P−E) hysteresis loop was obtained by applying a cyclic electric field along the out-of-plane direction, ranging from 0 to ±4 MV/cm with a field increment of 0.4 MV/cm.

The discrete quasi-two-dimensional mesh of $100\Delta x \times 2\Delta y \times 100\Delta z$ with a real grid space of $\Delta x=\Delta y=\Delta z=1.0$ nm was used in the simulation. Periodic boundary conditions were adopted to model the bulk ceramic. The numerical implementation of the phase-field model follows established methods in the literature,[4] and the normalized timestep was set to 0.004.

Weibull distribution method

This method is consistent with the standard widely adopted in this field.[5, 6] To determine the statistical E_b value of each composition, 10–12 ceramic samples were tested, with a thickness range of 50–90 μm. The Weibull distribution of the ceramics is calculated using the following formula

$$P_i=i/(n+1) \quad (7)$$

$$X_i=\ln(E_i) \quad (8)$$

$$Y_i=\ln(-\ln(1-P_i)) \quad (9)$$

$$P(E_i)=1-\exp((-E_i/E_b)^{\beta}) \quad (10)$$

where E_i represents the single breakdown value, i indicates the i^{th} measurement number, and n is the total number of tests for each sample (in this study, n = 10), E_i is the measured breakdown field, $P(E_i)$ presents the cumulative probability of electric breakdown at E_i, E_b is the statistical breakdown strength, which corresponds to the $P(E_i)$ is equal to 63.2%.The intersection point of the fitting line with Y_i = 0 is the theoretical value of E_b. The slope value of the fitting line represents the Voigt modulus β of the ceramic. β represents the dispersion degree of the E_b data, wherein a higher β value corresponds to a more concentrated distribution and a more uniform breakdown field strength.

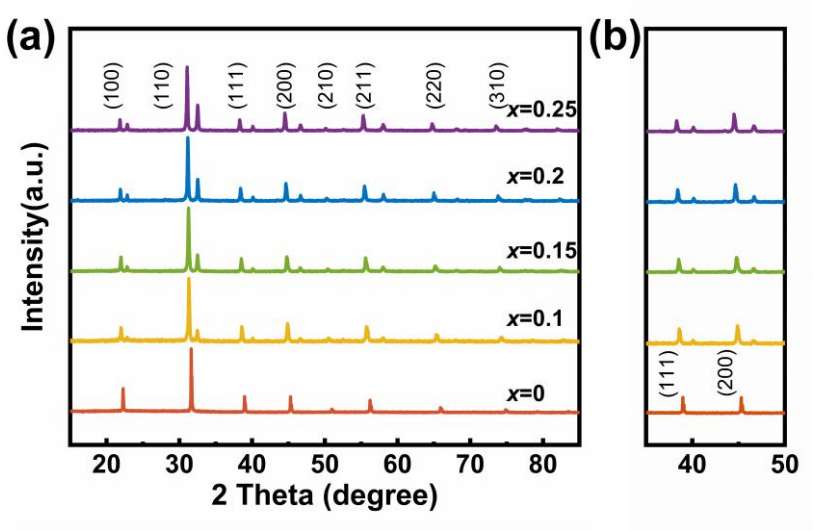

Fig. S1 (a) XRD patterns of 0.5BT−(0.5−*x*)BMT−*x*CZ ceramics and (b) an enlarged (200) profile of the $x = 0.2$ ceramic at room temperature.

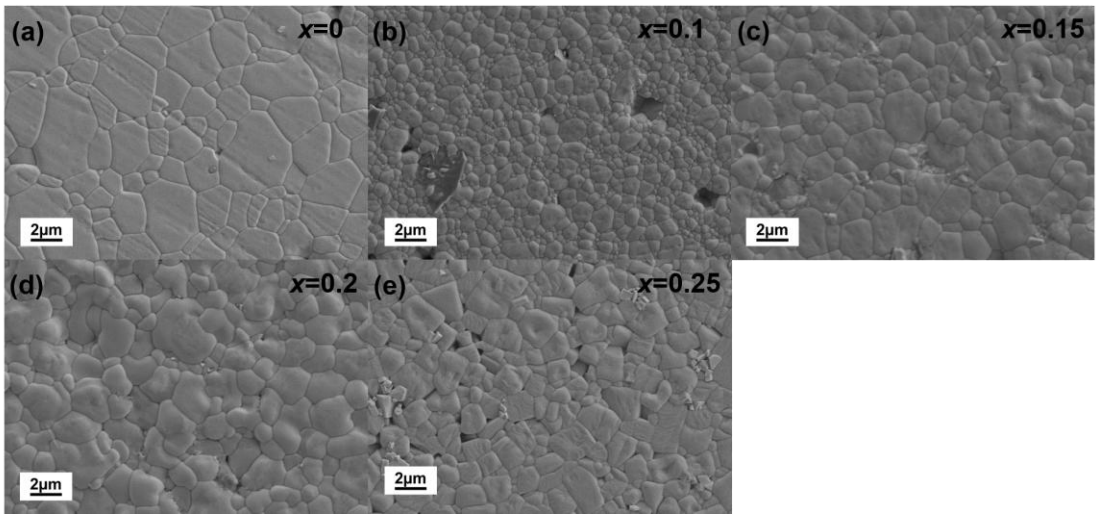

Fig. S2 Representative SEM surface morphologies of 0.5BT–(0.5–*x*)BMT–*x*CZ ceramics are shown for different compositions: (a) $x = 0$, (b) $x = 0.1$, (c) $x = 0.15$, (d) $x = 0.2$, and (e) $x = 0.25$.

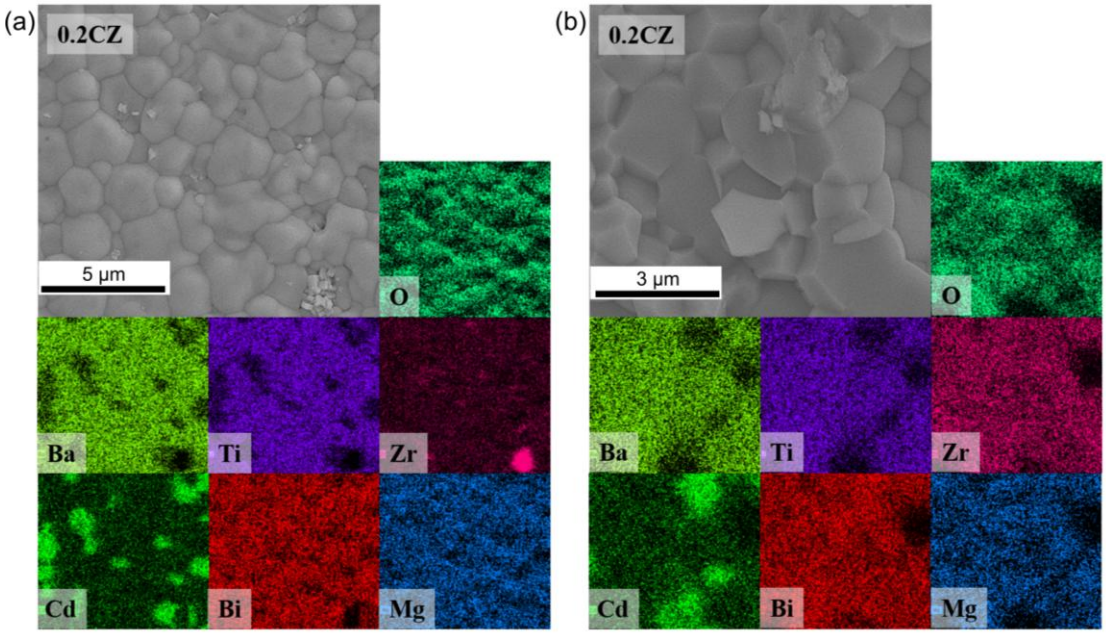

Fig. S3 SEM images of polished and thermally etched surfaces, accompanied by elemental mapping of dual-phase ferroelectric ceramics, are presented as follows: (a) surface morphology of the ceramic with x = 0.2, and (b) cross-sectional images of the ceramic with x = 0.2.

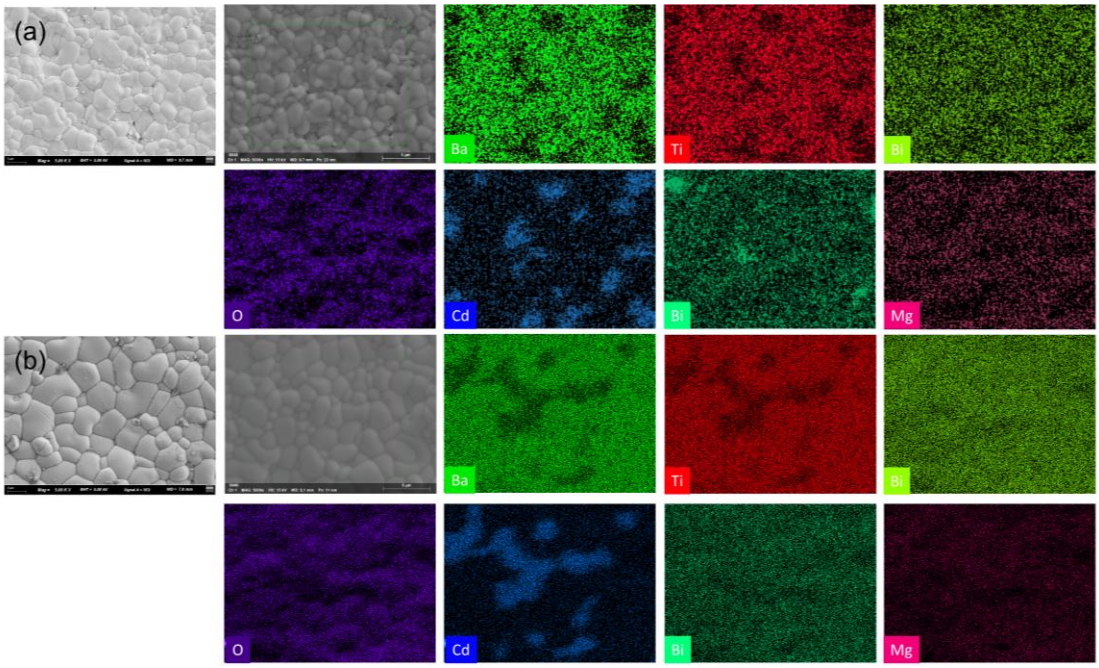

Fig. S4 SEM surface morphology and elemental distribution of the $x = 0.2$ ceramic: (a) before and (b) after high-temperature aging at 300 °C. These images reveal consistent elemental segregation at the grain level, with no evidence of further phase separation.

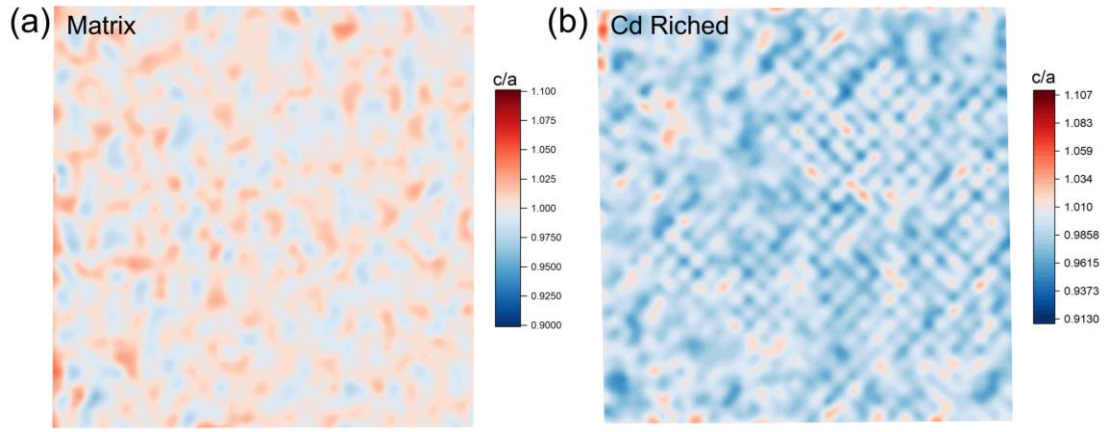

Fig. S5 Lattice distortion (*c/a* ratio) mapping of the ceramic with $x = 0.2$: (a) main phase; (b) Cd-rich secondary phase.

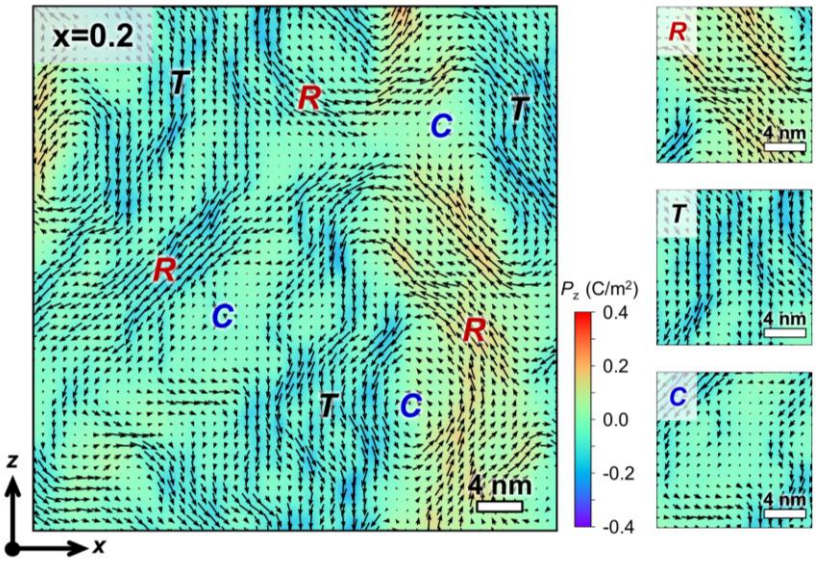

Fig. S6 Equilibrium domain configurations and dielectric phases of the $x = 0.2$ ceramic, as determined by phase-field simulation. The arrows represent the magnitude and orientation of the spontaneous polarization.

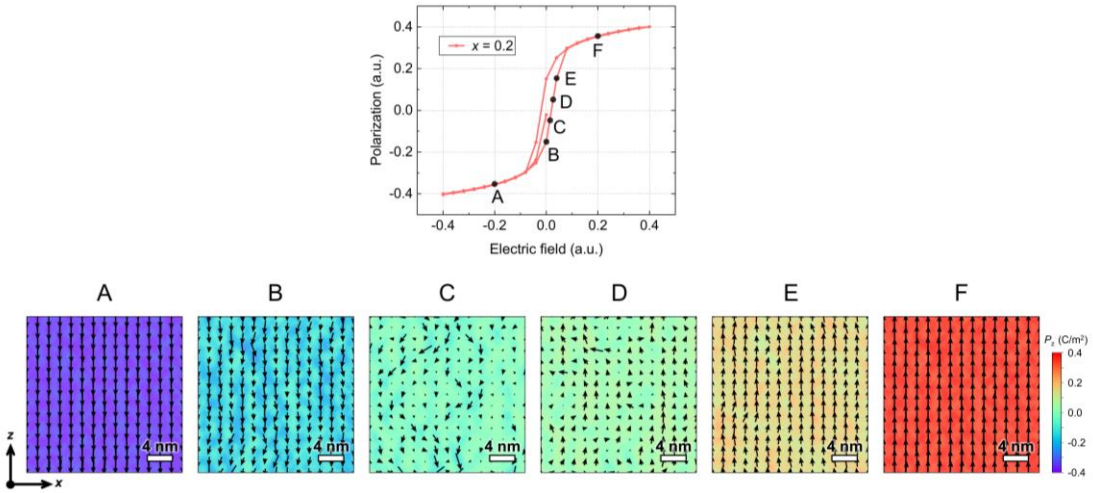

Fig. S7 Calculated *P*–*E* loop and dynamic evolution of polar configuration for $x = 0.2$ ceramic at room temperature based on phase-field simulation.

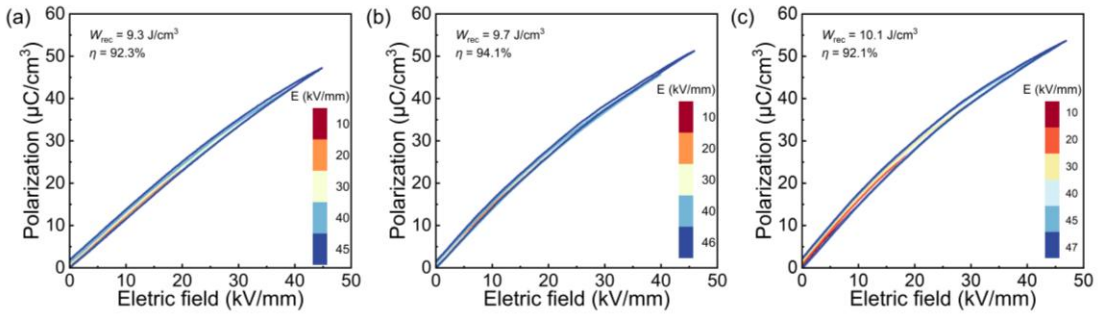

Fig. S8 Unipolar *P*–*E* loops of $x = 0.2$ ceramic under multiple measurements on three ceramics.

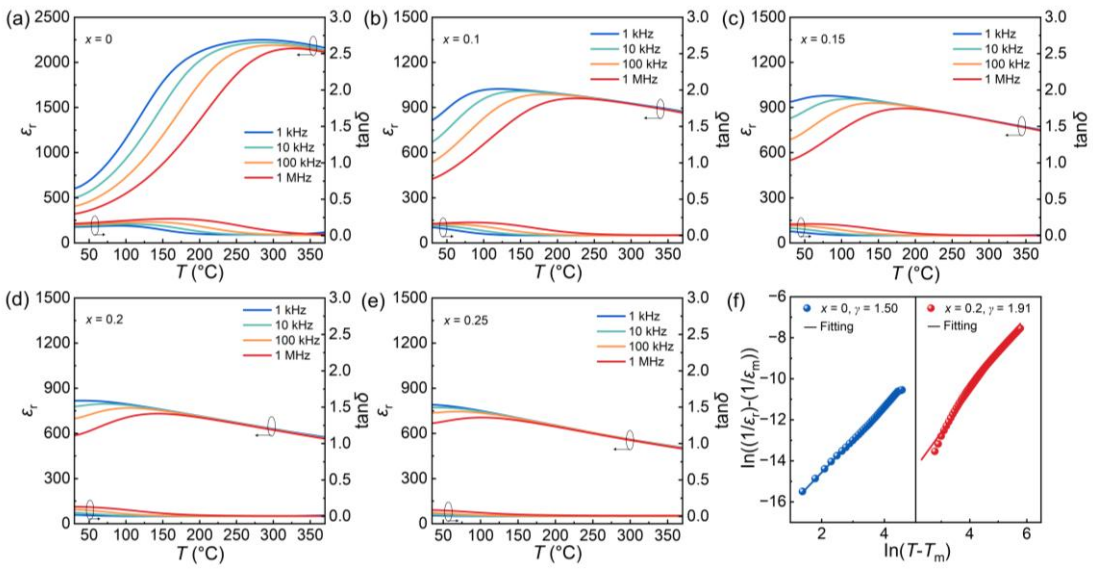

Fig. S9 Dielectric-temperature spectra of 0.5BT–(0.5–*x*)BMT–*x*CZ ceramics: (a) $x = 0$, (b) $x = 0.1$, (c) $x = 0.15$, (d) $x = 0.2$, (e) $x = 0.25$. (f) Relaxor degree (γ) of $x = 0$ and $x = 0.2$ ceramics.

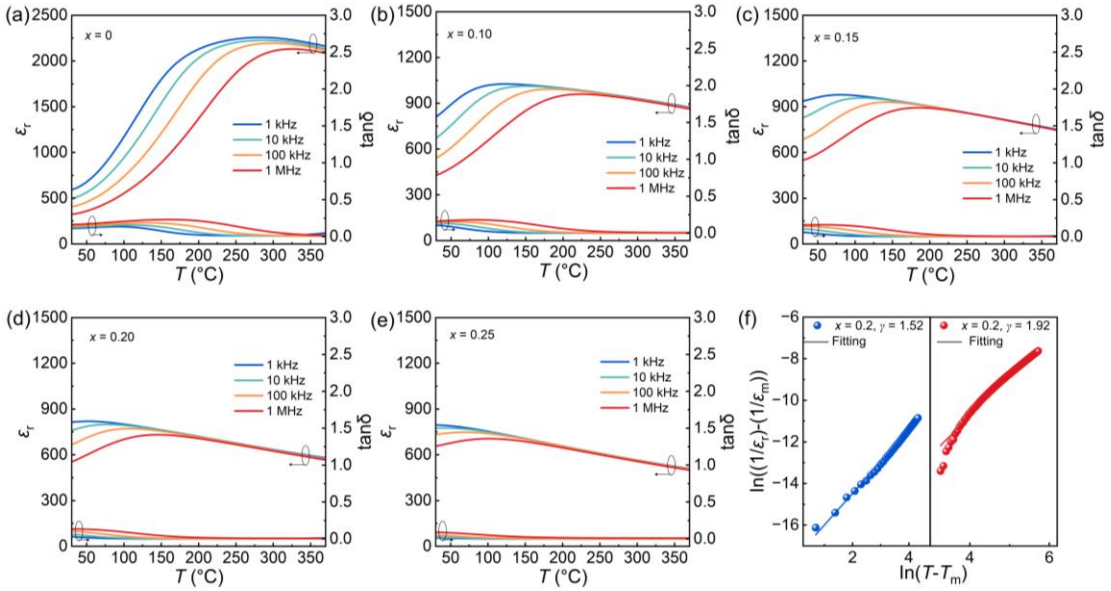

Fig. S10 Temperature-dependent dielectric spectra of 0.5BT–(0.5–*x*)BMT–*x*CZ ceramics after 10 months: (a) $x = 0$, (b) $x = 0.1$, (c) $x = 0.15$, (d) $x = 0.2$, (e) $x = 0.25$; (f) Relaxor degree (γ) for $x = 0$ and $x = 0.2$ ceramics. The dielectric–temperature spectra were remeasured on the same samples after 10 months, showing negligible changes and thereby confirming the long-term stability of the dielectric properties.

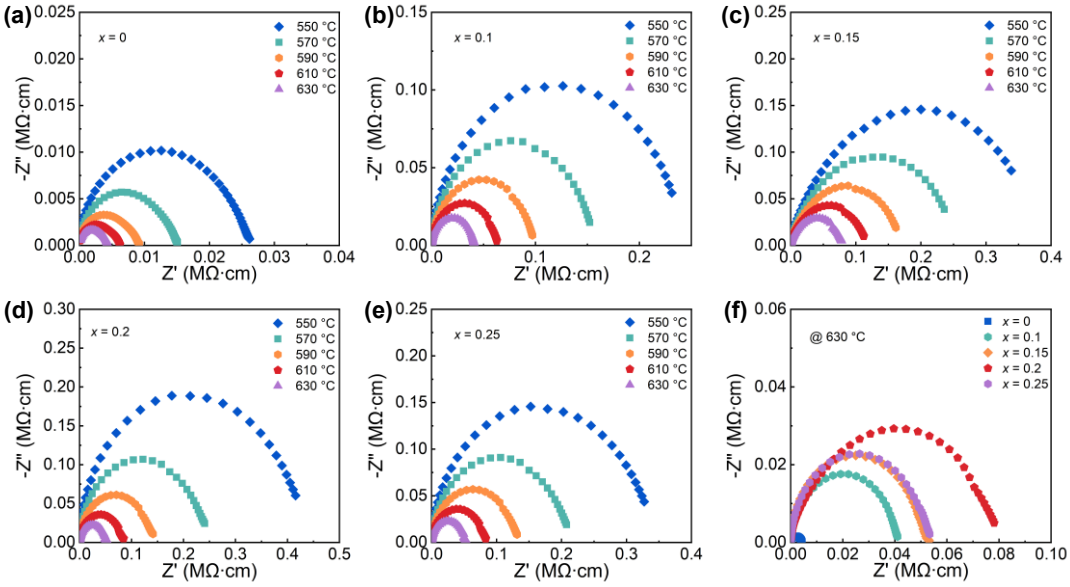

Fig. S11 Complex impedance spectra of 0.5BT–(0.5–*x*)BMT–*x*CZ ceramics measured between 550 and 630 °C: (a) $x = 0$, (b) $x = 0.1$, (c) $x = 0.15$, (d) $x = 0.2$, and (e) $x = 0.25$. (f) Impedance spectra of 0.5BT–(0.5–*x*)BMT–*x*CZ ceramics at 630 °C.

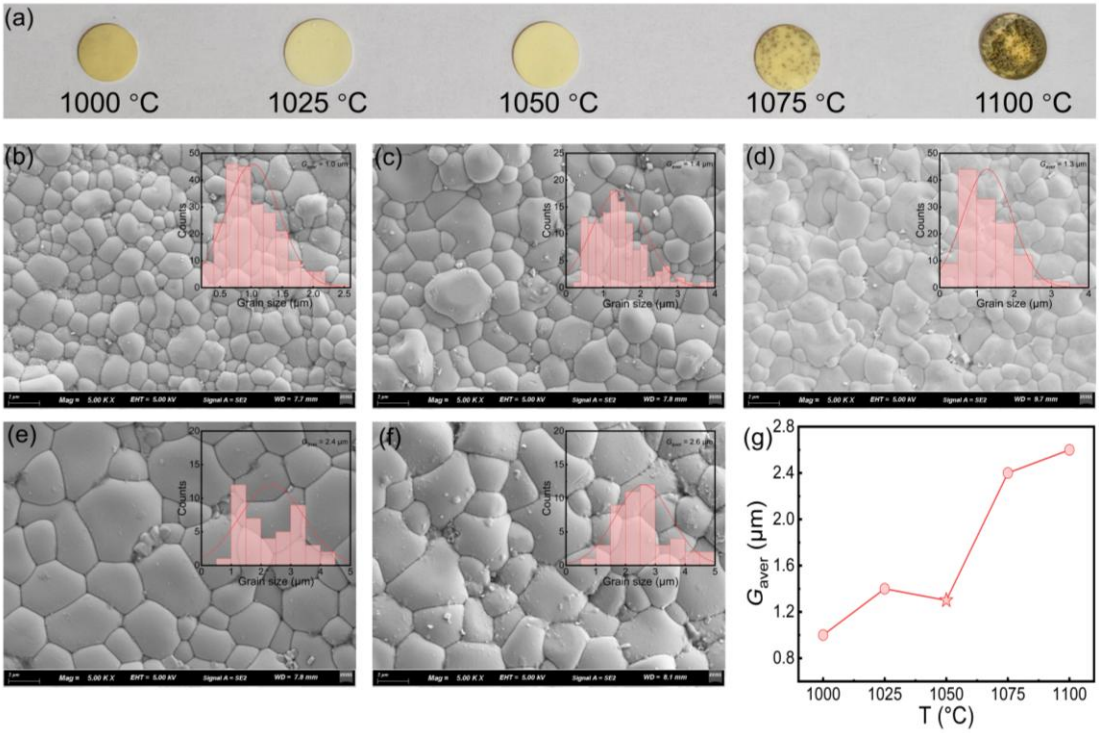

Fig. S12 (a) Digital photograph of the sample; (b–f) SEM morphologies and (g) grain size statistics of x = 0.2 ceramics sintered at 1000 °C, 1025 °C, 1050 °C, 1075 °C, and 1100 °C, respectively.

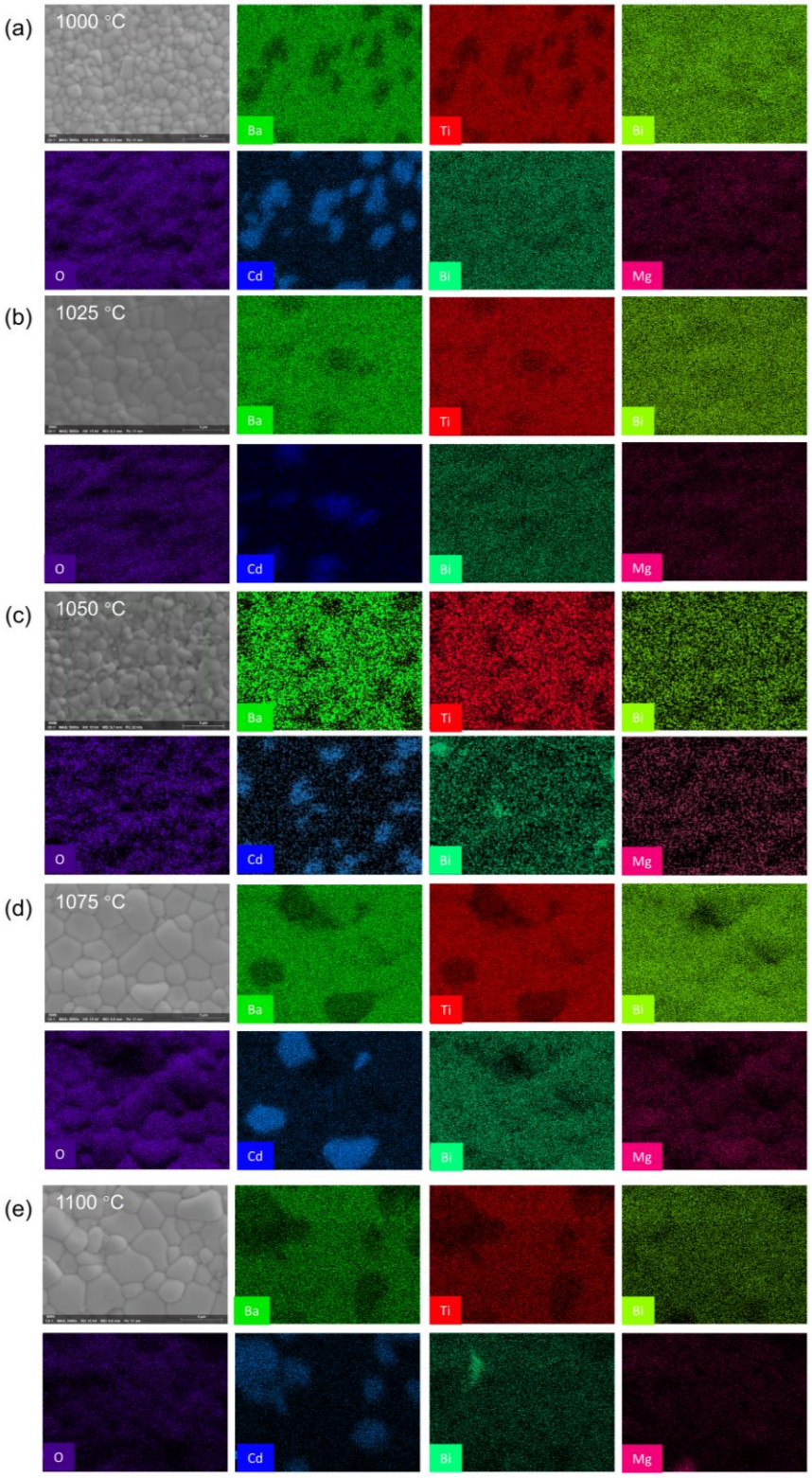

Fig. S13 SEM surface morphologies and corresponding elemental mappings of $x = 0.2$ ceramics sintered at (a) 1000 °C, (b) 1025 °C, (c) 1050 °C, (d) 1075 °C, and (e) 1100 °C.

Table S1. A comparison of W_{rec} and η between 0.5BT–0.3BMT–0.2CZ and other reported two-phase or multi-phase systems ceramics.[7-27]

Composition	W_{rec} (J/cm^3)	η (%)	Reference
0.94BT–0.06BMN	4.55	90	Ref. 7
0.45NBT–0.55SBT/6AlN	5.53	90	Ref. 8
BTAN–0.08	6.04	86.8	Ref. 9
0.92SBT–0.08BMH	3.5	92	Ref. 10
BF–BCZT	5.8	91.3	Ref. 11
BT–BMZ@SiO_2	3.41	85.1	Ref. 12
PLSZST–1 wt% ZnO	4.25	95.5	Ref. 13
0.3PLZS–Al_2O_3	13.2	74	Ref. 14
0.55BNT–0.45ST	4.94	88.45	Ref. 15
0.55(BNT–CS)–0.45SLT	4.55	83	Ref. 16
0.91BST–0.09NBN–VPP	8.5	93.4	Ref. 17
0.4BST–0.4BNT–0.2SZ	10	91	Ref. 18
00.62BF–0.3BT–0.08NZZ	10.5	87	Ref. 19
0.96(BKT–SBT)–0.04BMH	4.25	87	Ref. 20
BNTNN@0.8 wt% SiO_2	6.17	70	Ref. 21
BNNT–SBT–0.3Mn/BNNT–SBT–0.2Mn	6.03/5.84	71/85	Ref. 22
B–0.5SB	7.19	93.8	Ref. 23
BSTN–0.1Ta	12.2	89.5	Ref. 24
BNKLST	16.4	90	Ref. 25
0.5NN–0.5BNT core-shell	12.7	87.2	Ref. 26
SMT3	10.3	85.4	Ref. 27
0.5BT-0.3BMT–0.2CZ	9.7	92.8	This work

References

1. L. Q. Chen, Phase-Field Method of Phase Transitions/Domain Structures in Ferroelectric Thin Films: A Review, *J. Am. Ceram. Soc.*, 2008, **91**, 1835-1844.
2. J. Lin, X. Guo, B. Liu, Z. Qian, J. Chen, T. Sun, J. Liao, J. Li, Z. Hong, Y. Wu, X. Yu and Y. Huang, Exceptionally Large Thickness-Independent Longitudinal Strain in Lead-free Piezoceramics via Defect Dipole Engineering, *Adv. Funct. Mater.*, 2025, DOI: 10.1002/adfm.202522553, e22553.
3. L. Shu, X. Shi, X. Zhang, Z. Yang, W. Li, Y. Ma, Y.-X. Liu, L. Liu, Y.-Y.-S. Cheng, L. Wei, Q. Li, H. Huang, S. Zhang and J.-F. Li, Partitioning polar-slush strategy in relaxors leads to large energy-storage capability, *Science*, 2024, **385**, 204-209.
4. Y. L. Li, S. Y. Hu, Z. K. Liu and L. Q. Chen, Effect of substrate constraint on the stability and evolution of ferroelectric domain structures in thin films, *Acta Mater.*, 2002, **50**, 395-411.
5. M. Zhang, S. Lan, B. B. Yang, H. Pan, Y. Q. Liu, Q. H. Zhang, J. L. Qi, D. Chen, H. Su, D. Yi, Y. Y. Yang, R. Wei, H. D. Cai, H. J. Han, L. Gu, C.-W. Nan and Y.-H. Lin, Ultrahigh energy storage in high-entropy ceramic capacitors with polymorphic relaxor phase, *Science*, 2024, **384**, 185-189.
6. T. Li, S. Deng, R. Zhu, J. Yang, S. Xu, Y. Dong, H. Liu, C. Huo, P. Gao, Z. Luo, O. Diéguez, H. Huang, S. Liu, L.-Q. Chen, H. Qi and J. Chen, Ultrahigh-Efficiency Superior Energy Storage in Lead-Free Films with a Simple Composition, *J. Am. Chem. Soc.* , 2024, **146**, 1926-1934.
7. H. Yang, Z. Lu, L. Li, W. Bao, H. Ji, J. Li, A. Feteira, F. Xu, Y. Zhang, H. Sun, Z. Huang, W. Lou, K. Song, S. Sun, G. Wang, D. Wang and I. M. Reaney, Novel BaTiO3-Based, Ag/Pd-Compatible Lead-Free Relaxors with Superior Energy Storage Performance, *ACS Appl. Mater. Interfaces*, 2020, **12**, 43942-43949.
8. D. You, H. Tan, Z. Yan, H. Gao, S. Chen, W. Ma, P. Fan, N.-M.-A. Tran, Y. Liu, D. Salamon and H. Zhang, Enhanced Dielectric Energy Storage Performance of $0.45Na_{0.5}Bi_{0.5}TiO_3$-$0.55Sr_{0.7}Bi_{0.2}TiO_3$/AlN 0–3 Type Lead-Free Composite Ceramics, *ACS Appl. Mater. Interfaces*, 2022, **14**, 17652-17661.

9. M. Liu, H. Liu, Z. Liu, Z. Hu, K. Dai, S. Yan, Z. Hu and G. Wang, Superior energy-storage performance in $BaTiO_3$-$AgNbO_3$ binary relaxor via the competitions of multiple polar orders, *Acta Mater.*, 2025, **289**, 120943.
10. X. Kong, L. Yang, Z. Cheng and S. Zhang, Enhanced Energy-Storage Properties and Good Temperature Stability in $0.92(Sr_{0.7}Bi_{0.2})TiO_3$–$0.08Bi(Mg_{0.5}Hf_{0.5})O_3$ Relaxor Ferroelectric Ceramic, *Adv. Energy Sustainability Res.*, 2021, **2**, 2100015.
11. K. Xi, Y. Li, M. Zheng, M. Zhu and Y. Hou, Exceptional Energy-Storage in Low-Temperature Sintered BCZT-Based Ceramics Featuring Polymorphic Relaxor Phase Coupled With Dual-Distribution Secondary Inclusions, *Adv. Funct. Mater.*, 2025, **35**, e11375.
12. Q. Yuan, F. Z. Yao, S. D. Cheng, L. Wang, Y. Wang, S. B. Mi, Q. Wang, X. Wang and H. Wang, Bioinspired Hierarchically Structured All-Inorganic Nanocomposites with Significantly Improved Capacitive Performance, *Adv. Funct. Mater.*, 2020, **30**, 2000191.
13. H. Zhao, R. Xu, M. J. Wang, G. Wang, H. C. Sun, X. Z. Wang, Q. S. Zhu, X. Y. Wei, Y. J. Feng and Z. Xu, Excellent Energy Storage Performance of ZnO doped $(Pb,La)(Zr,Sn,Ti)O_3$ Based Antiferroelectric Ceramics at an Ultra-Low Sintering Temperature of 940 °C, *Adv. Funct. Mater.*, 2024, **34**, 2316674.
14. N. Luo, X. He, C. Xu, Z. Chen, K. Zhao, Z. Cen, X. Chen, D. Shan, Y. Liu, Z. Liu, H. Xie, Y. Zhu, H. Huang, J. F. Li and S. Zhang, Ordering-Structured Antiferroelectric Composite Ceramics for Energy Storage Applications, *Adv. Mater.*, 2025, **37**, 2420258.
15. Y. Jiao, S. Song, F. Chen, X. Zeng, X. Wang, C. Song, G. Liu and Y. Yan, Energy storage performance of 0.55Bi0.5Na0.5TiO3-0.45SrTiO3 ceramics doped with lanthanide elements (Ln = La, Nd, Dy, Sm) using a viscous polymer processing route, *Ceram. Int.*, 2022, **48**, 10885-10894.
16. Z. Zhai, Q. Zhou, Z. Peng, L. Zhou, F. Zhang, D. Wu, T. Yang, X. Chao and Z. Yang, Enhanced energy storage properties and relaxation behavior of BNT-based ceramics via A-sites substitution, *Ceram. Int.*, 2025, **51**, 6220-6227.

17. W. Wang, Y. Yang, J. Qian, W. Shi, Y. Huang, R. Jing, L. Zhang, Z. Pan, V. Laletin, V. Shur, J. Zhai and L. Jin, Advancing energy storage properties in barium titanate-based relaxor ferroelectric ceramics through a stagewise optimization strategy, *Chem. Eng. J.*, 2024, **488**, 151043.
18. F. Yang, Y. Bao, B. Zeng, J. Wu, X. Li, Y. Sun, Y. Chen and G. Wang, Excellent energy storage properties in ZrO_2 toughened $Ba_{0.55}Sr_{0.45}TiO_3$-based relaxor ferroelectric ceramics via multi-scale synergic regulation, *Chem. Eng. J.*, 2024, **493**, 152624.
19. G. Wang, J. Li, X. Zhang, Z. Fan, F. Yang, A. Feteira, D. Zhou, D. C. Sinclair, T. Ma, X. Tan, D. Wang and I. M. Reaney, Ultrahigh energy storage density lead-free multilayers by controlled electrical homogeneity, *Energy Environ. Sci.*, 2019, **12**, 582-588.
20. R. Kang, Z. Wang, Y. Zhao, Y. Li, Y. Hu, X. Hao, L. Zhang and X. Lou, Enhanced energy storage performance of $Bi_{0.5}K_{0.5}TiO_3$-based ceramics via composition modulation, *J. Alloys Compd.*, 2023, **935**, 167999.
21. C. Zhu, A. Li, X. Li, S. Li, Z. Feng, Z. Cai, P. Feng and X. Wang, Ultra-stable dielectric properties and enhanced energy storage density of BNT-NN-based ceramics via precise core-shell structure controlling, *J. Alloys Compd.*, 2025, **1010**, 177556.
22. Y. Zhang, C. Yu, X. Zhou, Y. Jiang, G. Xue, Y. Zhang and D. Zhang, Phase structure and grain boundary engineering of BNT-based relaxor ferroelectric ceramics for high performance dielectric capacitors, *J. Energy Storage*, 2025, **115**, 115961.
23. W. Shi, L. Zhang, R. Jing, Y. Huang, F. Chen, V. Shur, X. Wei, G. Liu, H. Du and L. Jin, Moderate Fields, Maximum Potential: Achieving High Records with Temperature-Stable Energy Storage in Lead-Free BNT-Based Ceramics, *Nano Micro Lett.*, 2024, **16**, 091.
24. J. Liu, Y. Jiang, W. Zhang, X. Cheng, P. Zhao, Y. Zhen, Y. Hao, L. Guo, K. Bi and X. Wang, Ferroelectric tungsten bronze-based ceramics with high-energy storage performance via weakly coupled relaxor design and grain boundary

optimization, *Nat. Commun.*, 2024, **15**, 8651.

25. T. Wei, J. Zou, X. Zhou, M. Song, Y. Zhang, C. Nan, Y. Lin and D. Zhang, High-entropy assisted capacitive energy storage in relaxor ferroelectrics by chemical short-range order, *Nat. Commun.*, 2025, **16**, 807.
26. H. Yu, T. Hu, H. Wang, H. Qi, J. Wu, R. Zhang, W. Fang, X. Shi, Z. Fu, L. Chen and J. Chen, Design of polymorphic heterogeneous shell in relaxor antiferroelectrics for ultrahigh capacitive energy storage, *Nat. Commun.*, 2025, **16**, 886.
27. X. Dong, T. Hu, X. Wu, J. Yin, Z. Fu and J. Wu, A novel lead-free relaxor with endotaxial nanostructures for capacitive energy storage, *SusMat*, 2023, **4**, 116-125.